

Biomedical x-ray imaging with a GaAs photon-counting detector: A comparative study

Cite as: APL Photonics 5, 106108 (2020); <https://doi.org/10.1063/5.0020262>

Submitted: 29 June 2020 . Accepted: 29 September 2020 . Published Online: 15 October 2020

 J. Scholz,  L. Birnbacher,  C. Petrich, M. Riedel, L. Heck,  S. Gkoumas, T. Sellerer, K. Achterhold, and  J. Herzen



View Online



Export Citation



CrossMark

ARTICLES YOU MAY BE INTERESTED IN

[Tubular optical microcavities based on rolled-up photonic crystals](#)

APL Photonics 5, 106106 (2020); <https://doi.org/10.1063/5.0022862>

[Perfectly absorbing dielectric metasurfaces for photodetection](#)

APL Photonics 5, 101304 (2020); <https://doi.org/10.1063/5.0019883>

[Ultrafast single-shot optical vector network analyzer based on coherent time-stretch](#)

APL Photonics 5, 106109 (2020); <https://doi.org/10.1063/5.0022121>

APL Photonics
Become a member of the
Early Career Advisory Board

[Find out how](#)

Biomedical x-ray imaging with a GaAs photon-counting detector: A comparative study

Cite as: APL Photon. 5, 106108 (2020); doi: 10.1063/5.0020262
Submitted: 29 June 2020 • Accepted: 29 September 2020 •
Published Online: 15 October 2020



J. Scholz,^{1,a)}  L. Birnbacher,^{1,2,b)}  C. Petrich,^{1,c)}  M. Riedel,^{1,3,d)} L. Heck,^{1,e)} S. Gkoumas,^{4,f)}  T. Sellerer,^{1,g)}
K. Achterhold,^{1,h)} and J. Herzen^{1,i)} 

AFFILIATIONS

¹Chair of Biomedical Physics, Department of Physics and Munich School of BioEngineering, Technical University of Munich, 85748 Garching, Germany

²Department of Diagnostic and Interventional Radiology, School of Medicine & Klinikum Rechts der Isar, Technical University of Munich, 81675 München, Germany

³Institute of Materials Research, Helmholtz-Zentrum Geesthacht, 21502 Geesthacht, Germany

⁴DECTRIS Ltd., 5405 Baden, Switzerland

^{a)} Author to whom correspondence should be addressed: josef.scholz@tum.de

^{b)} Electronic mail: lorenz.birnbacher@ph.tum.de

^{c)} Electronic mail: ch.petrich@tum.de

^{d)} Electronic mail: mirko.riedel@tum.de

^{e)} Electronic mail: lisa.heck@tum.de

^{f)} Electronic mail: spyridon.gkoumas@dectris.com

^{g)} Electronic mail: thorsten.sellerer@tum.de

^{h)} Electronic mail: klaus.achterhold@tum.de

ⁱ⁾ Electronic mail: julia.herzen@tum.de

ABSTRACT

Photon-counting detectors provide several potential advantages in biomedical x-ray imaging including fast and readout noise free data acquisition, sharp pixel response, and high dynamic range. Grating-based phase-contrast imaging is a biomedical imaging method, which delivers high soft-tissue contrast and strongly benefits from photon-counting properties. However, silicon sensors commonly used in photon-counting detectors have low quantum efficiency for mid- to high-energies, which limits high throughput capabilities when combined with grating-based phase contrast imaging. In this work, we characterize a newly developed photon-counting prototype detector with a gallium arsenide sensor, which enables imaging with higher quantum efficiency, and compare it with a silicon-based photon-counting and a scintillation-based charge integrating detector. In detail, we calculated the detective quantum efficiency (DQE) of all three detectors based on the experimentally measured modulation transfer function, noise power spectrum, and photon fluence. In addition, the DQEs were determined for two different spectra, namely, for a 28 kVp and a 50 kVp molybdenum spectrum. Among all tested detectors, the gallium arsenide prototype showed the highest DQE values for both x-ray spectra. Moreover, other than the comparison based on the DQE, we measured an *ex vivo* murine sample to assess the benefit using this detector for grating-based phase contrast computed tomography. Compared to the scintillation-based detector, the prototype revealed higher resolving power with an equal signal-to-noise ratio in the grating-based phase contrast computed tomography experiment.

© 2020 Author(s). All article content, except where otherwise noted, is licensed under a Creative Commons Attribution (CC BY) license (<http://creativecommons.org/licenses/by/4.0/>). <https://doi.org/10.1063/5.0020262>

I. INTRODUCTION

In contrast to widely used scintillation-based detectors, photon-counting detectors use direct conversion semiconductor

sensors, which convert incident x-rays directly into an electrical signal. Photon-counting technology features several advantages for x-ray related imaging applications including a sharp pixel response,

high dynamic range, electronic noise free readout, and spectral energy discrimination.^{1–4}

Originally, only silicon sensors were used in photon-counting detectors, since silicon wafer production has been pushed intensively by the semiconductor microelectronics industry. In addition, although silicon sensors achieve extremely high crystal quality, their stopping power is limited due to the low atomic number ($Z = 14$). The resulting comparably low quantum efficiency of silicon based photon-counting in contrast to scintillation-based detectors, however, limits a wider range of application in x-ray imaging. Recent advances have made sensor materials with higher atomic numbers such as gallium arsenide (GaAs) ($Z = 31/33$) and cadmium telluride (CdTe) ($Z = 48/52$) available for photon-counting technology to increase the conversion efficiency.⁴ However, the current manufacturing process of CdTe and GaAs sensors is still challenging and results in impurities and dislocations within the sensors, which can cause non-uniform pixel responses.^{5,6}

Scientific applications in life and material sciences have been using the advantages of photon counting-detectors in x-ray diffraction, scattering, and imaging applications such as protein crystallography for years.^{7–9} Even first clinical prototype applications of photon-counting technology have recently been achieved.^{10–12}

A biomedical imaging technology, which highly benefits from photon-counting technology, is x-ray grating-based phase contrast imaging (GBPCI). GBPCI is an interferometry based x-ray imaging technique, which allows us to measure extremely small refraction angles arising from fine electron density variations of a given material, and delivers increased soft-tissue contrast in comparison to well-known attenuation based imaging.^{13–15} Although a variety of phase contrast methods have been developed for highly-coherent synchrotron sources, the grating-based phase contrast approach has successfully been adapted by low-brilliance laboratory x-ray sources.¹⁶ In laboratory GBPCI setups, three x-ray gratings are combined to form a so-called Talbot–Lau interferometer. GBPCI provides quantitative data accessibility^{17–19} and has proven itself in several preclinical applications, ranging from phase contrast mammography^{20,21} to high-sensitivity grating-based phase contrast computed tomography (GBPC-CT) of atherosclerotic plaque, kidney, or breast samples.^{22–24}

In order to achieve high soft-tissue contrast with GBPCI, high angular sensitivity is required for the detection of small refraction angle variations. The absence of readout noise and the provided high dynamic range of photon-counting detectors turned out to be essential for high-sensitivity GBPCI.^{25–27} The advancement of high-sensitivity GBPCI still suffers from the low quantum efficiency of the utilized silicon sensors, since it results in long measurement times. In addition to that, higher spatial resolution would be necessary for a wider range of GBPCI application. Those issues could be solved with a high- Z and small pixelated sensor for GBPCI.

In this work, we present a newly developed photon-counting detector—the DECTRIS SANTIS 0808 GaAs HR prototype—equipped with a GaAs sensor. In detail, we characterize the SANTIS prototype on the basis of detective quantum efficiency (DQE) and compare it to two additional detectors, a photon-counting detector—a DECTRIS EIGER S 500 k—with a silicon sensor, and a scintillation-based detector—a PerkinElmer Dexela 1512—with a gadolinium oxysulfide (Gadox) screen. The DQE is a standard for detector characterization²⁸ and describes how effectively an

imaging system transfers the spatial frequency components of an incident signal compared to an ideal detector. The DQE thereby is composed of the measured incident photon fluence Q , the noise power spectrum (NPS), and the modulation transfer function (MTF) of the respective detector. We calculated the DQE for all three detectors at two different x-ray spectra, a standard mammography spectrum, namely a molybdenum (Mo) 28 kVp spectrum including specific filtration of 30 μm Mo and 2 mm aluminum, and a Mo 50 kVp spectrum as used for GBPCI. The second part of this manuscript shows the imaging performance of the SANTIS prototype in GBPC-CT. We performed two GBPC-CT scans of an *ex vivo* murine sample with the SANTIS and the Dexela detector under otherwise equivalent experimental conditions. Furthermore, we compared the tomographic phase contrast data qualitatively in terms of spatial resolution and quantitatively based on the signal-to-noise-ratio (SNR).

II. MATERIALS AND METHODS

A. X-ray detectors

Three detectors are used for this characterization: The SANTIS 0808 GaAs HR prototype (DECTRIS Ltd., Baden, Switzerland) photon-counting detector, an EIGER S 500 k (DECTRIS Ltd., Baden, Switzerland) photon-counting detector, and a Dexela 1512 (PerkinElmer, Inc., Waltham, United States) scintillation based energy-integrating detector. The two photon-counting detectors are equipped with a 500 μm thick gallium GaAs (SANTIS) and a 450 μm thick silicon (EIGER) sensor.

A general advantage of photon-counting detectors is that incident photons are directly converted into charge, which is amplified and digitized by a bump bonded application-specific integrated circuit (ASIC). The ability to apply thresholds to generated charge pulses allows us to cut off electronic noise in photon-counting detectors. A threshold was therefore placed at 7 keV for the SANTIS and the EIGER detector for all measurements within this work in order to keep the measurements comparable.

The Dexela detector is a scintillation based CMOS detector equipped with a Gadox sensor usually used in digital mammography.^{29,30} In contrast to photon-counting detectors, this integrating detector accumulates charge before readout³¹ and noise cannot be cut off. All detectors have nearly the same pixel size of 75 μm . More detailed technical specifications of all three detectors are listed in Table I. Unfortunately, the sensor thickness of the Dexela detector could not be specified in Table I, since neither the information about it is available in the literature, nor does the manufacturer provide it.

B. X-ray spectra

The DQE related measurements within this work were carried out with two different x-ray spectra: A Mo 50 kVp and a Mo 28 kVp spectrum. Both spectra were generated with a Rigaku RA-Micro7 HFMR tabletop rotating anode x-ray generator. The 50 kVp spectrum was filtered with the gratings of a Talbot–Lau interferometer and a 4 cm thick water container (cf. Sec. II D for further information), as used for GBPC-CT. The second spectrum was achieved with the generator operating at 28 kVp and an additional filtration of 30 μm Mo and 2 mm aluminum. Those settings are standard settings for mammographic radiation quality (RQA-M2)

TABLE I. Technical specifications of the DECTRIS SANTIS 0808 GaAs HR prototype, the DECTRIS EIGER S 500 k, and the Dexela 1512 x-ray detector imaging systems.

	SANTIS 0808 GaAs HR prototype	EIGER S 500k	Dexela 1512
Sensor material	GaAs	Si	Gadox
Sensor thickness (μm)	500	450	N/S
Pixel size (μm)	75×75	75×75	74.8×74.8
Sensitive area (mm)	77.25×77.2	77×38.6	114.4×145
Pixels	1030×1028	1030×514	1536×1944
ADC resolution	16 bit	12 bit	14 bit
Readout time	Continuous, zero dead time	Continuous, 3 μs dead time	N/S
Thresholds	2	1	N/A

according to the International Electrotechnical Commission (IEC).³² The tube current was set the maximum value of 24 mA for both x-ray spectra.

C. Detective quantum efficiency (DQE) measurement

The DQE is a standard measure to characterize the performance of x-ray imaging systems in medical x-ray imaging.²⁸ It is a relative measure, which describes how the signal-to-noise ratio (SNR) of a radiation field is transferred by an imaging system.³³ The DQE depends on the spatial frequencies u and v and can be expressed according to the IEC as follows:²⁸

$$DQE(u, v) = MTF^2(u, v) \frac{W_{in}(u, v)}{W_{out}(u, v)}. \quad (1)$$

Here, $MTF(u, v)$ is the spatial frequency dependent MTF, which describes how effectively spatial frequencies are transferred by an imaging system. $W_{in}(u, v)$ is the input NPS of the radiation field at the detector surface and $W_{out}(u, v)$ the digital output NPS of the imaging device.

As in Ref. 28, $W_{in}(u, v)$ is equal to the photon fluence Q of the incoming radiation field. $W_{out}(u, v)$ is the spectral decomposition of the noise variance [$NPS(u, v)$] of a detector and hence a measure for detector noise. In consequence, the DQE [Eq. (1)] can be rearranged to

$$DQE(u, v) = MTF^2(u, v) \frac{Q}{NPS(u, v)}, \quad (2)$$

which sets the detector specific measures $MTF(u, v)$ and $NPS(u, v)$ in relation to the photon fluence Q of an incident radiation field.

DQE measurements were conducted for all detectors (cf. Sec. II A) with a Mo 28 kVp and a Mo 50 kVp spectrum (cf. Sec. II B), respectively. Data acquisition and processing of DQE related quantities are specified by the IEC²⁸ and described in detail in the following.

1. Conversion function

The first parameter to calculate the DQE is the photon fluence Q (photons/mm²). On the one hand, this quantity is needed to directly calculate the DQE [cf. Eq. (2)], and on the other hand to express the detector output in units of photons/mm². Detector output and photon fluence Q have to be measured for different exposure levels to obtain the conversion function. In case of a linear detector response, determining a conversion function simplifies to the

determination of a conversion factor. The photon fluence Q can be calculated via

$$Q = K_a \cdot \left[\int \Phi(E) \left(\frac{\mu_{tr}}{\rho} \right) E dE \right]^{-1}, \quad (3)$$

where K_a is the measured air kerma dose value in J/kg at the detector surface, $\Phi(E)$ is the measured and normalized x-ray spectra, and μ_{tr}/ρ is the mass energy transfer coefficient.³⁴

Both x-ray spectra were measured with an energy-dispersive x-ray detector, a X-123 complete x-ray spectrometer with Si-PIN Detector (Amptek, Inc., Bedford, United States), and corrected according to the specific quantum efficiency of the sensor. The corresponding K_a values were acquired with a Nomex dosimeter (PTW GmbH, Freiburg, Germany) at the detector surface position. The photon mass energy transfer coefficients were taken from Ref. 35. To obtain the conversion factors for each spectrum and detector, the measured data points were fitted linearly. The photon fluence values Q were determined to be 0.44×10^6 photons/mm² for the 50 kVp spectrum and 1.25×10^6 photons/mm² for the 28 kVp spectrum.

2. Noise-power spectrum (NPS)

The NPS is the squared amplitude of the Fourier transform of an image and shows the image frequency amplitudes as a function of the spatial frequency. For this purpose, overlapping regions of interest (ROIs) with a size of 256×256 pixels with an overlap of 128 pixels in x- and y-directions were chosen. The number of ROIs has been selected according to reach a minimum of 4×10^6 independent pixels. The two-dimensional NPS can be calculated via

$$NPS(u_n, v_k) = \frac{\Delta x \Delta y}{M \cdot N_x \cdot N_y} \sum_{m=1}^M \left| \sum_{i=1}^{N_x} \sum_{j=1}^{N_y} (I(x_i, y_j) - S(x_i, y_j)) \right. \\ \left. \times \exp(2\pi i(u_n x_i + v_k y_j)) \right|^2, \quad (4)$$

where Δx and Δy denote the pixel pitch in x- and y-directions, M the number of ROIs, and N_x and N_y the ROI size in numbers of pixels. $I(x, y)$ is the linearized data, or more precisely the raw detector data to which the conversion factors have been applied. Additionally, a 2D-polynomial fit $S(x, y)$ can be applied to correct the data for non-uniform irradiation.²⁸ This step was omitted in our case since corrections on non-uniform irradiation have been made in

the course of flat field correction, which is equivalent to a division by a flat image normalized to its mean value. The 1D-NPS can be calculated by averaging 14 pixel lines around the vertical as well as the horizontal axis in the 2D-NPS.²⁸ Data within spatial frequency intervals of $f_{\text{int}} = 0.01/\text{pixelpitch}$ (mm) around defined spatial frequencies (multiples of 0.5 lp/mm) were averaged to determine the final NPS.²⁸ To facilitate a direct comparison of the individual NPS for two different spectra with a different photon fluence, the NPS in Sec. III A 1 is normalized to the respective photon fluence. The normalized NPS (NNPS) is obtained by dividing the NPS by the squared photon fluence $|Q|^2$.

3. Modulation transfer function (MTF)

To measure the MTFs of the above mentioned detectors, an approach using a sharp and straight edge was used to calculate the MTF from a smeared edge profile in comparison to an ideally sharp edge.²⁸ A tungsten edge (99.96% chemical purity) was placed as close as possible to the detector surface. Putting the edge profile close to the detector surface aims at eliminating any contribution of the x-ray source spot and thus to solely measure the MTF of the corresponding x-ray detector. Furthermore, a slight tilt of a few degrees of the edge profile against the pixel grid ensures a denser sampling of the edge.²⁸ Measurements were conducted with the edge profile orientated along the vertical and horizontal orientation of the detector pixel matrices in order to obtain MTFs in both directions. All acquired images were flatfield corrected in terms of dividing the raw images by flatfield images and normalized subsequently.

Combining all data points in each detector row or line into one profile yields the edge spread function (ESF), which is obtained by plotting the normalized pixel values against their distances to the edge profile. The derivative of the ESF yields the line spread function (LSF), from which the MTF can be calculated by taking the real part of Fourier transform of the LSF. The final MTF, which considers both horizontal and vertical properties, was obtained by averaging both unidirectional MTFs.²⁸ Considering an ideal detector with infinite small resolution, the MTF along all spatial frequencies will not deviate from one. For a detector with a finite pixel size, the ideal MTF can be calculated by the Fourier transforming a rectangle function with width d corresponding to the detector pixel size. Consequently, the ideal MTF of a detector with finite pixel size d is given by a sinc function as follows:

$$MTF_{\text{ideal}}(u) = \frac{\sin(\pi du)}{\pi du}, \quad (5)$$

with u being the spatial frequency. In the further course of the work, the ideal MTF is used as a reference for the experimentally determined MTFs (cf. Sec. III A 2).

In addition to the MTF measurements, Siemens star images were acquired to further highlight and visualize the differences in resolving power performance of the SANTIS and the Dexela detector. The EIGER photon-counting detector was excluded from this comparison because it was assumed to exhibit a very similar MTF progression to the SANTIS prototype. The employed Siemens star has a maximum spatial frequency of 16.0 lp/mm with a lead foil thickness of 0.03 mm. Again, the Siemens star pattern was positioned as close as possible to the detector and the data were flatfield corrected and normalized.

D. GBPC-CT measurement

In the GBPC-CT measurement, an *ex vivo* murine sample was measured with the SANTIS and the Dexela detector (cf. Sec. II A). The datasets were compared subsequently based on detail resolution and image noise.

In a laboratory-based differential phase contrast (DPC) setup, where mainly incoherent x-ray sources are used, a set of three gratings is applied to form a Talbot–Lau interferometer (more detailed information can be found in Ref. 16). The present interferometer is composed of two absorption and one phase grating with grating periods of 5.4 μm . As the central component, the phase grating is applied to create an interference pattern. Since the modulations of this pattern are too small to be resolved directly by the detector, an absorption grating is required for sampling of the interference pattern. To meet the coherence requirements for interferometry, which usually is not met with standard laboratory sources, a second absorption grating is necessary to split an extended x-ray source into an array of individually coherent, but mutually incoherent line sources. In the current setting, the three gratings are arranged in a symmetrical configuration with inter-grating distances of 856 mm at an overall length of 1.71 m. The phase grating is designed to produce a phase-shift of π rad at a design energy of 27 keV.²⁶

Additionally, a water container of 4 cm thickness is placed in the beam path to avoid phase-wrapping artifacts and to prevent beam-hardening effects in CT imaging.^{17,36,37} Although the mean energy (37 keV) of the filtered 50 kVp spectrum differs from the design energy of the interferometer (27 keV), the gain in photon flux at this higher acceleration voltage has an overall positive effect on image noise. In the current configuration, the experimental setup reaches an effective pixel size of 35.8 μm using the aforementioned x-ray detectors (cf. Sec. II A).

The murine sample was fixated in formalin inside an Eppendorf Tube[®] and has already been used in previous studies. Animal care and experimental protocols were conducted in accordance with German animal protection laws and approved by the Institutional Animal Care and Use Committee at the Technical University Munich.

The SANTIS prototype was compared only to the Dexela detector, since the SANTIS and EIGER detectors, except for differences in noise transfer, are assumed to exhibit a very similar imaging performance.²⁷ Both CT measurements were conducted with a Mo 50 kVp spectrum and an *ex vivo* murine sample serving as the biological specimen. In sum, 1200 projections over 360° were acquired for both measurements using the phase-stepping technique.¹⁵ Each projection was acquired with 11 phase steps and an exposure time of 5 s each step, which results in a measurement time of about two days for one tomography. Despite this long measuring time, neither photon flux instabilities of the source nor position fluctuations of the source spot could be observed. The individual projection images were processed using a fast Fourier transform (FFT) algorithm and a subsequent offset-correction was applied to the DPC images. A filtered backprojection algorithm employing a Hilbert filter was chosen to reconstruct the 3D phase contrast volumes from the DPC projection data.³⁸ Moreover, all measurements were conducted with a PMMA rod attached to the sample required for effective energy calibration, so that the electron density can be calculated.¹⁷ In order to assess the image quality of both detectors in a GBPC-CT setup, the electron density resolution (standard deviation) and

signal-to-noise-ratio (SNR) are used. From the reconstructed electron density volumes, a three-dimensional volume with a size of $100 \times 100 \times 100$ pixels inside the PMMA rod was selected to determine the PMMA electron density standard deviation and mean value for each detector.

III. RESULTS AND DISCUSSION

A. DQE measurements

1. NPS

Figure 1 shows the NNPS of the SANTIS and EIGER photon-counting detectors as well as the Dexela flat-panel, each for two different x-ray spectra. The NNPS recorded with the 50 kVp spectrum and a Talbot–Lau interferometer along with a water container are indicated with solid lines, whereas the dashed lines represent the NNPS recorded with the Mo/Al filtered Mo 28 kVp spectrum. For all three detectors, the NNPS mean amplitudes show higher values when measured with the 50 kVp spectrum, which appears legitimate due to expected decreased effective quantum efficiency toward higher photon energies. Deviations from a uniform frequency distribution, specifically a more prominent presence of lower spatial frequencies for the present case, are due to multiple detection of incident photons by several surrounding pixels. In scintillation based detectors such as the Dexela flat-panel, this usually occurs due to the light produced in the scintillation layer spreads out over several pixels.³⁹ For direct converting photon-counting detectors such as the SANTIS and the EIGER detector, a similar effect occurs due to charge diffusion in the conversion layer referred to as charge sharing.^{40,41} As shown in Fig. 1, this effect is much more pronounced with the scintillation based Dexela detector than with both photon-counting detectors.

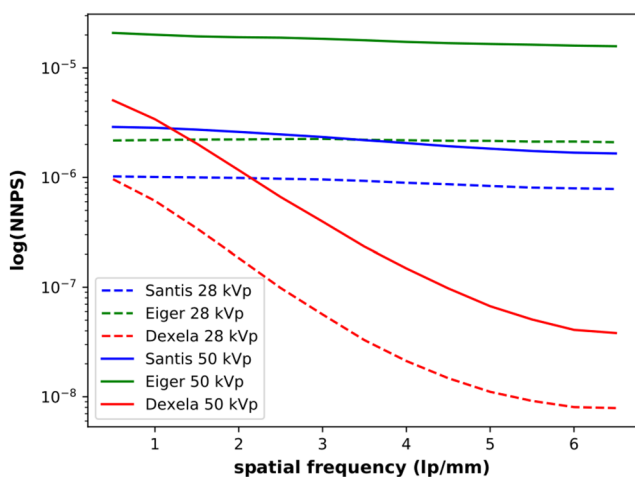


FIG. 1. Normalized noise power spectra (NNPS) of the SANTIS prototype, the EIGER, and the Dexela detector at two different X-ray spectra. The NNPS for the Mo 50 kVp spectrum (filtered with the gratings of the Talbot–Lau interferometer and 4 cm water) are indicated with solid lines, and the NNPS measured with the Mo 28 kVp spectrum (filtered with $30 \mu\text{m}$ Mo and 2 mm aluminum) are indicated with dashed lines.

2. MTF

The results of the MTF measurements for all three detectors are visualized in Fig. 2. Compared to the SANTIS (blue lines) and EIGER (green lines) photon-counting detectors, the Dexela (red lines) indirect conversion flat-panel detector exhibits a steep drop in MTF with increasing spatial frequency for both spectra. In Table II, the spatial frequency values of all detectors and both x-ray spectra are listed for 50% MTF and 10% MTF. The MTFs of both photon-counting detectors do not fall below 10% MTF and the SANTIS prototype does not even fall below 50% MTF for the 28 kVp spectrum. Compared to the ideal MTF for a pixel size of $75 \mu\text{m}$ (cf. Fig. 2, black solid line), all three detectors show a lower MTF progression. Deviations from the ideal MTF can be explained by crosstalk between neighboring detector pixels. With respect to the values shown in Fig. 2, the MTF of the Dexela detector drops much faster than those of both photon-counting detectors, which indicates a strong influence of shared light in the scintillation layer of the Dexela detector. For the photon-counting detectors, the MTFs reach higher values toward higher spatial frequencies with the 28 kVp spectrum than with the 50 kVp spectrum. This behavior can be explained by an increase in shared charges between neighboring pixels and an increased escape x-ray traveling distance due to higher photon energies. For the Dexela detector, this effect is reversed, which can be explained by a higher penetration depth of incident photons toward higher energies.

Figures 3(a) and 3(b) depict image sections of the Siemens star measured with the SANTIS and the Dexela detector. Both transmission images are normalized to values between zero and one. Blue rimmed boxes additionally show magnified regions around the Siemens star center plate and the red quadrants indicate the position

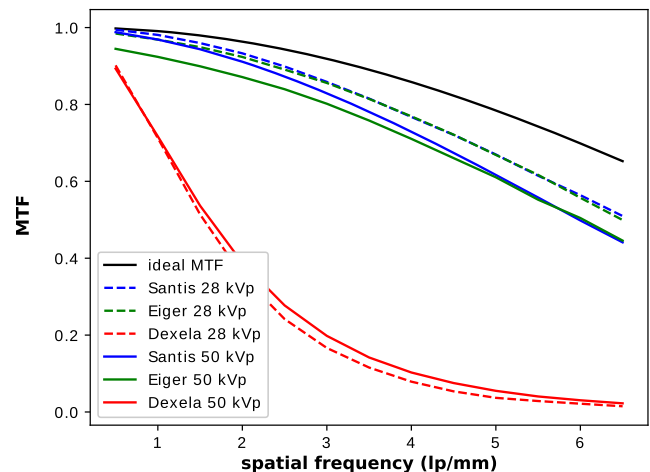


FIG. 2. MTFs of the three detectors for the 28 kVp (dashed lines) and the 50 kVp (solid lines) spectrum in comparison to the MTF of an ideal detector. The MTFs of the SANTIS (blue lines) and the EIGER (green lines) detector look quite similar and decrease to approximately 50% (28 kVp spectrum) and 44% (50 kVp spectrum) up to Nyquist frequency. In contrast, the MTF of the Dexela detector drops much faster (10% MTF at 3.71 lp/mm at 28 kVp and 4.05 lp/mm at 50 kVp) right up to 3% MTF at Nyquist frequency. In contrast, the ideal MTF for a detector with a pixel size of $75 \mu\text{m}$ (black solid line) only decreases to 64% MTF up to Nyquist frequency.

TABLE II. Spatial frequency values at MTF(50%) and at MTF(10%) of the SANTIS, EIGER, and Dexela detectors for the 28 kVp and the 50 kVp x-ray spectrum.

	28 kVp		50 kVp	
	MTF(50%) (lp/mm)	MTF(10%) (lp/mm)	MTF(50%) (lp/mm)	MTF(10%) (lp/mm)
SANTIS	N/A	N/A	5.98	N/A
EIGER	6.49	N/A	6.04	N/A
Dexela	1.54	3.71	1.62	4.05

of the Nyquist frequency. Incipient blurring of structures recognizable below the Nyquist frequency appears with the Dexela detector [cf. Fig. 3(b)]. In contrast, these structures remain visible when measured with the SANTIS prototype, even above the Nyquist frequency. The remaining structures above the Nyquist frequency can be attributed to aliasing artifacts, which occur when periodic structures are sampled above the Nyquist frequency. The Siemens star performance of both detectors mirrors the results of previous MTF measurements (cf. Fig. 2). As the steep decrease in the Dexela MTF indicates, high frequency structures are blurred. In contrast, the slow progression within the SANTIS MTF maintains the resolution of fine image structures.

3. DQE

The DQE can now be calculated according to Eq. (2) with the previous results for the photon fluence, the MTF, and the NPS.

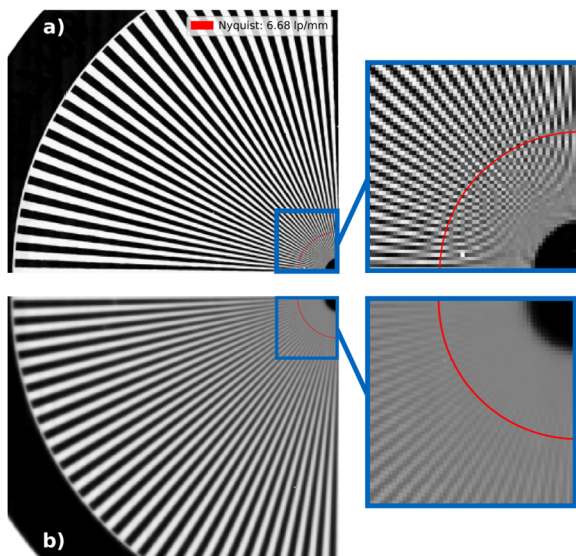


FIG. 3. Measured Siemens star sections with additional zoom-ins close to the center plate of the SANTIS (a) and the Dexela detector (b). The Nyquist frequency of both detectors is marked with a red solid line. The influence of the detector MTF is not apparent below the Nyquist frequency in case of the SANTIS prototype (a), whereas blurring of the structures is clearly recognizable for the Dexela detector (b). However, due to the sharp pixel response of the SANTIS prototype, aliasing of regular patterns above the Nyquist frequency becomes prominent.

The results of all DQE measurements with the SANTIS (blue lines), EIGER (green lines), and Dexela (red lines) detectors are shown in Fig. 4. The progressions of the DQEs measured at 50 kVp are indicated with solid lines, and those measured at 28 kVp with dashed lines. Additionally, the DQE values at zero spatial frequency [DQE(0)] and at the Nyquist frequency [DQE(N)] of all three detectors for both x-ray spectra are listed in Table III. It is visible that the EIGER detector, except for high spatial frequencies with the 28 kVp spectrum, in general, shows the lowest DQE values followed by the Dexela flat-panel detector for both x-ray spectra. The highest experimentally determined DQE for each spectrum is obtained with the SANTIS prototype. Comparing both DQEs for each detector, the DQE measured with the 28 kVp spectrum provides higher values than those obtained with the 50 kVp spectrum. According to Eq. (2) and considering a decrease in effective quantum efficiency toward higher x-ray photon energies, this relation mainly follows the corresponding NNPS depicted in Fig. 1.

B. Grating-based phase contrast computed tomography (GBPC-CT) measurement

In order to evaluate the imaging performance of the SANTIS prototype specifically to GBPC-CT, an *ex vivo* murine sample was measured with both the Dexela and the SANTIS prototype. Based

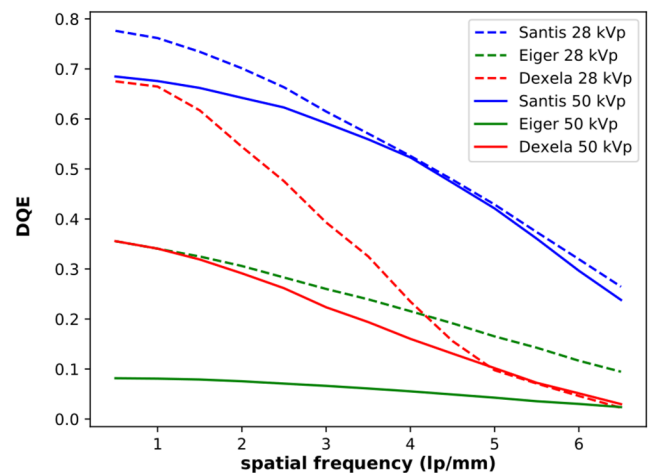


FIG. 4. The DQEs of the three detectors for two different x-ray spectra. DQEs measured with the Mo 50 kVp spectrum are indicated with solid lines, and the DQEs measured with the Mo 28 kVp spectrum are indicated with dashed lines.

TABLE III. The DQE values at zero spatial frequency [DQE(0)] and at the Nyquist frequency [DQE(N)] of the SANTIS, EIGER, and Dexela detectors for the 28 kVp and the 50 kVp x-ray spectrum.

	28 kVp		50 kVp	
	DQE(0) (%)	DQE(N) (%)	DQE(0) (%)	DQE(N) (%)
SANTIS	77.6	26.5	68.5	23.8
EIGER	35.6	9.5	8.2	2.4
Dexela	67.5	2.2	35.6	3.0

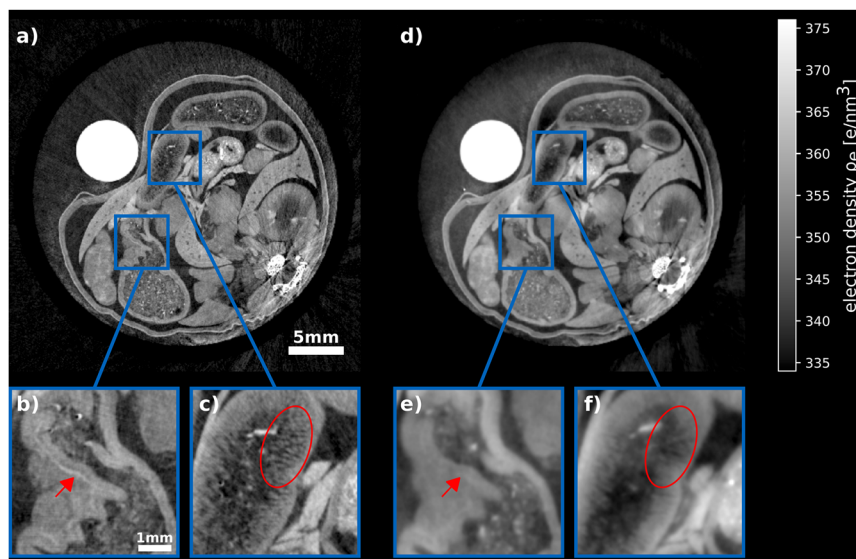


FIG. 5. (a)–(f): Tomographic GBPC-CT slices of the abdominal area of the *ex vivo* murine sample measured with the SANTIS (a) and the Dexela detector (d). Both measurements were conducted with the Mo 50 kVp spectrum filtered with the Talbot–Lau interferometer and a 4 cm water container. The images were recorded with an effective voxel size of $35.8\ \mu\text{m}$ and are displayed in electron density values in units of e/nm^3 . A PMMA rod [upper left in (a) and (d)], which is needed for calibration of quantitative values, was placed additionally next to the sample. Subfigures (b) and (e) depict magnifications of the gastric area and subfigures (c) and (f) show a magnification of the intestine. In contrast to the Dexela images [(e) and (f)], features inside the gastric wall [(b), red arrow] and intestinal villi [(c), red ellipse] are resolved with the SANTIS prototype.

on the DQE measurements, the EIGER detector was excluded from this comparison because it was assumed to produce a similar image quality apart from image noise. The main difference in the DQE of the SANTIS and EIGER detectors is due to their difference in NPS. Since both detectors have an almost identical MTF progression, no difference in resolving power is to be expected between both detectors for phase contrast tomography. Due to the large differences in NPS between the SANTIS and EIGER detectors, it can be assumed that the phase contrast tomography data of the EIGER detector will have a comparable resolution but higher image noise.

Figure 5 shows matched axial slices of the abdominal area of a murine sample measured with the SANTIS prototype [Fig. 5(a)] and the Dexela flat-panel [Fig. 5(d)]. The tomographic data have an effective voxel size of $35.8\ \mu\text{m}$ and are displayed in electron density (ρ_e) values with units of e/nm^3 . The white circles on the upper left connote PMMA rods, which are necessary for electron density calibration. Magnified sections of the gastric area [cf. Figs. 5(b) and 5(e)] and the intestine [cf. Figs. 5(c) and 5(f)] are visualized in the blue rimmed boxes [cf. Figs. 5(b), 5(c), 5(e), and 5(f)] for the SANTIS prototype and the Dexela flat-panel detector, respectively. Compared to the SANTIS prototype [Fig. 5(a)], the GBPC-CT slice of the Dexela detector [Fig. 5(d)] generally appears less noisy and streak artifacts arising from the backbone are pronounced less distinct. This can be explained by the influence of the different detector MTFs as measured, which is discussed in Sec. III A 2. Whereas high spatial frequencies are preserved by the SANTIS photon-counting detector, a fast decreasing MTF for the Dexela charge-integrating detector introduces blurring to the images. In comparison, the SANTIS prototype unveils image features such as additional structures inside the gastric wall [red arrow, Fig. 5(b)] and intestinal villi [red ellipse, Fig. 5(c)], which are not resolved in the Dexela images [Figs. 5(e) and 5(f)], although measured at the same effective pixel size. Standard deviations and mean values of the electron density ρ_e have been extracted for both detectors within a volume of $100 \times 100 \times 100$ pixels inside the PMMA rod. For the SANTIS prototype, the electron density $\rho_{e,\text{PMMA}}$ was found to be $(386.32 \pm 1.66)\ \text{e}/\text{nm}^3$ and

for the Dexela detector $(386.24 \pm 1.67)\ \text{e}/\text{nm}^3$, which results in similar SNR values of 232.85 (SANTIS) and 231.94 (Dexela). This means that within identical conditions, images generated with the SANTIS prototype reveal finer structures with a slightly higher SNR when compared to a scintillation-based Dexela detector.

IV. CONCLUSION

In this work, we assessed the performance of the DECTRIS SANTIS 0808 GaAs HR prototype photon-counting detector regarding its application for high-resolution and high-sensitivity grating-based phase contrast imaging. The selection of this detector was based on criteria such as readout noise, a pixel size that is as small as possible, sufficiently large sensitive area, and high quantum efficiency. The comparison detectors were selected based on their favored application for phase contrast imaging and their use in medical imaging.

First, we compared the experimentally determined DQE of this newly developed GaAs based photon-counting detector with a silicon sensor based DECTRIS EIGER S 500 k photon-counting and a Dexela 1512 flat-panel detector with a Gadox scintillator layer. The DQE was determined for two different x-ray spectra, a Mo 28 kVp and a Mo 50 kVp spectrum. The 28 kVp spectrum was additionally filtered with 2 mm aluminum and $30\ \mu\text{m}$ molybdenum resulting in a mammographic standard spectrum. The second spectrum was specifically chosen to fit our phase contrast imaging setup. In order to calculate the DQE for each detector, the photon fluence Q , the noise power spectrum (NPS), and the modulation transfer function (MTF) were measured for both spectra. Both photon-counting detectors show nearly equally distributed image frequencies in their measured NPS or NNPS, whereas the Dexela NPS is mainly dominated by low spatial frequencies (cf. Fig. 1). In general, the NNPS amplitudes of the EIGER are higher than those of the SANTIS prototype. This points to a higher quantum efficiency of the SANTIS prototype. Concerning the MTF measurements, the curve progression for both spectra (visualized in Fig. 2) presents a clear advantage

of both photon-counting detectors over the Dexela detector regarding the resolving power. Slightly better results were achieved with the SANTIS photon-counting detector for the 50 kVp spectrum compared to the EIGER detector. The SANTIS photon-counting detector reached the best DQE results for both spectra and the EIGER detector showed the lowest DQE values (cf. Fig. 4). Due to identical photon fluence and similar MTFs within both spectra, the difference in DQE originates from a difference in quantum efficiency of the gallium arsenide and the silicon sensor, which can be seen from the respective NNPS (cf. Fig. 1). The DQE of the Dexela detector is also moderately high at lower spatial frequencies, however, declining fast with higher spatial frequencies due to the MTF shown in Fig. 2.

In the second part of this work, we performed an exemplary GBPC-CT scan of a murine sample. We measured an *ex vivo* murine sample with both the SANTIS and the Dexela detector under otherwise identical conditions. In the tomographic slices of the sample (cf. Fig. 5), the imaging results of the SANTIS prototype present higher spatial resolution indicated by the presence of finer structures in the abdominal area, which cannot be differentiated with the Dexela detector to the same degree due to a lower MTF (cf. Fig. 2). The SNR of the tomographic electron density values does not differ much between the Dexela (SNR = 231.94) and the SANTIS prototype (SNR = 232.85). This means that although phase contrast imaging with the Dexela detector profits from noise reduction due to intrinsic blurring (lower MTF), results with higher resolution can be obtained with the SANTIS prototype at almost equal signal-to-noise ratio.

In conclusion, the DECTRIS SANTIS 0808 GaAs HR prototype has highly beneficial properties for our GBPC-CT application. Compared to the silicon-based photon-counting and the scintillation-based detectors used within the scope of this work, the GaAs prototype photon-counting detector showed the highest DQE progression for both, the Mo 28 kVp and the Mo 50 kVp spectrum. The underlying high quantum efficiency, sharp pixel response, and noise properties render this detector interesting not only for phase contrast micro CT but also for other flux or dose limited applications such as breast imaging in general, micro-, and breast CT.⁵⁰ As this range of application could not entirely be covered in the context of this work, further investigation in this direction would be interesting in future work.

ACKNOWLEDGMENTS

We acknowledge financial support through the Deutsche Forschungsgemeinschaft (DFG), Research Training Group, under Grant GRK 2274. This work was carried out with the support of the Karlsruhe Nano Micro Facility (KNMF, www.kit.edu/knmf), a Helmholtz Research Infrastructure at Karlsruhe Institute of Technology (KIT), and DECTRIS Ltd. (Switzerland).

DATA AVAILABILITY

The data that support the findings of this study are available from the corresponding author upon reasonable request.

REFERENCES

¹S. Gkoumas, T. Thuering, A. G. Taboada, A. Jensen, M. Rissi, C. Broennimann, and P. Zambon, "Dose-independent near-ideal DQE of a 75 μm pixel GaAs

photon counting spectral detector for breast imaging," *Proc. SPIE* **10948**, 109480V (2019).

²P. Kraft, A. Bergamaschi, C. Broennimann, R. Dinapoli, E. F. Eikenberry, B. Henrich, I. Johnson, A. Mozzanica, C. M. Schlepütz, P. R. Willmott, and B. Schmitt, "Performance of single-photon-counting PILATUS detector modules," *J. Synchrotron Radiat.* **16**, 368–375 (2009).

³C. Ponchut, J. M. Rigal, J. Clément, E. Papillon, A. Homs, and S. Petitdemange, "MAXIPIX, a fast readout photon-counting X-ray area detector for synchrotron applications," *J. Instrum.* **6**, C01069 (2011).

⁴C. Brönnimann and P. Trüb, "Hybrid pixel photon counting X-ray detectors for synchrotron radiation," in *Synchrotron Light Sources and Free-Electron Lasers: Accelerator Physics, Instrumentation and Science Applications* (Springer International Publishing, Cham, 2014), pp. 1–29.

⁵C. Szeles, "CdZnTe and CdTe materials for X-ray and gamma ray radiation detector applications," *Phys. Status Solidi B* **241**, 783–790 (2004).

⁶D. Pennicard, S. Smoljanin, F. Pithan, M. Sarajlic, A. Rothkirch, Y. Yu, H. P. Liermann, W. Morgenroth, B. Winkler, Z. Jeneli, H. Stawitz, J. Becker, and H. Graafsma, "LAMBDA 2m GaAs—A multi-megapixel hard X-ray detector for synchrotrons," *J. Instrum.* **13**, C01026 (2018).

⁷B. Henrich, A. Bergamaschi, C. Broennimann, R. Dinapoli, E. F. Eikenberry, I. Johnson, M. Kobas, P. Kraft, A. Mozzanica, and B. Schmitt, "PILATUS: A single photon counting pixel detector for X-ray applications," *Nucl. Instrum. Methods Phys. Res., Sect. A* **607**, 247–249 (2009).

⁸M. Guizar-Sicairos, I. Johnson, A. Diaz, M. Holler, P. Karvinen, H.-C. Stadler, R. Dinapoli, O. Bunk, and A. Menzel, "High-throughput ptychography using eiger: Scanning X-ray nano-imaging of extended regions," *Opt. Express* **22**, 14859–14870 (2014).

⁹A. Förster, S. Brandstetter, and C. Schulze-Briese, "Transforming X-ray detection with hybrid photon counting detectors," *Philos. Trans. R. Soc., A* **377**, 20180241 (2019).

¹⁰M. J. Willeminck, M. Persson, A. Pourmorteza, N. J. Pelc, and D. Fleischmann, "Photon-counting CT: Technical principles and clinical prospects," *Radiology* **289**, 293–312 (2018).

¹¹N. Berger, M. Marcon, N. Saltybaeva, W. A. Kalender, H. Alkadhi, T. Frauenfelder, and A. Boss, "Dedicated breast computed tomography with a photon-counting detector: Initial results of clinical in vivo imaging," *Invest. Radiol.* **54**, 409–418 (2019).

¹²C. H. McCollough, K. Boedeker, D. Cody, X. Duan, T. Flohr, S. Halliburton, J. Hsieh, R. Layman, and N. J. Pelc, "Principles and applications of multi-energy CT: Report of AAPM task group 291," *Med. Phys.* **47**, e881 (2020).

¹³R. Fitzgerald, "Phase-sensitive X-ray imaging," *Phys. Today* **53**, 23–26 (2000).

¹⁴A. Momose, "Phase-sensitive imaging and phase tomography using X-ray interferometers," *Opt. Express* **11**, 2303–2314 (2003).

¹⁵T. Weitkamp, A. Diaz, C. David, F. Pfeiffer, M. Stampanoni, P. Cloetens, and E. Ziegler, "X-ray phase imaging with a grating interferometer," *Opt. Express* **13**, 6296–6304 (2005).

¹⁶F. Pfeiffer, T. Weitkamp, O. Bunk, and C. David, "Phase retrieval and differential phase-contrast imaging with low-brilliance X-ray sources," *Nat. Phys.* **2**, 258–261 (2006).

¹⁷J. Herzen, T. Donath, F. Pfeiffer, O. Bunk, C. Padeste, F. Beckmann, A. Schreyer, and C. David, "Quantitative phase-contrast tomography of a liquid phantom using a conventional x-ray tube source," *Opt. Express* **17**, 10010–10018 (2009).

¹⁸M. Willner, M. Viermetz, M. Marschner, K. Scherer, C. Braun, A. Fingerle, P. Noël, E. Rummeny, F. Pfeiffer, and J. Herzen, "Quantitative three-dimensional imaging of lipid, protein, and water contents via X-ray phase-contrast tomography," *PLoS One* **11**, e0151889 (2016).

¹⁹L. Birnbacher, M. Willner, M. Marschner, D. Pfeiffer, F. Pfeiffer, and J. Herzen, "Accurate effective atomic number determination with polychromatic grating-based phase-contrast computed tomography," *Opt. Express* **26**, 15153–15166 (2018).

²⁰M. Stampanoni, Z. Wang, T. Thüning, C. David, E. Roessl, M. Trippel, R. A. Kubik-Huch, G. Singer, M. K. Hohl, and N. Hauser, "The first analysis and clinical evaluation of native breast tissue using differential phase-contrast mammography," *Invest. Radiol.* **46**, 801–806 (2011).

²¹K. Scherer, K. Willer, L. Gromann, L. Birnbacher, E. Braig, S. Grandl, A. Sztroákay-Gaul, J. Herzen, D. Mayr, K. Hellerhoff, and F. Pfeiffer, "Toward

- clinically compatible phase-contrast mammography,” *PLoS One* **10**, e0130776 (2015).
- ²²H. Hetterich, M. Willner, S. Fill, J. Herzen, F. Bamberg, A. Hipp, U. Schüller, S. Adam-Neumair, S. Wirth, M. Reiser, F. Pfeiffer, and T. Saam, “Phase-contrast CT: Qualitative and quantitative evaluation of atherosclerotic carotid artery plaque,” *Radiology* **271**, 870–878 (2014).
- ²³M. Braunagel, L. Birnbacher, M. Willner, M. Marschner, F. De Marco, M. Viermetz, S. Notohamiprodjo, K. Hellbach, S. Auweter, V. Link, C. Woischke, M. F. Reiser, F. Pfeiffer, M. Notohamiprodjo, and J. Herzen, “Qualitative and quantitative imaging evaluation of renal cell carcinoma subtypes with grating-based X-ray phase-contrast CT,” *Sci. Rep.* **7**, 45400 (2017).
- ²⁴K. Hellerhoff, L. Birnbacher, A. Sztrókay-Gaul, S. Grandl, S. Auweter, M. Willner, M. Marschner, D. Mayr, M. F. Reiser, F. Pfeiffer, and J. Herzen, “Assessment of intraductal carcinoma in situ (DCIS) using grating-based X-ray phase-contrast CT at conventional X-ray sources: An experimental ex-vivo study,” *PLoS One* **14**, e0210291 (2019).
- ²⁵M. Bech, O. Bunk, C. David, P. Kraft, C. Brönnimann, E. F. Eikenberry, and F. Pfeiffer, “X-ray imaging with the PILATUS 100k detector,” *Appl. Radiat. Isot.* **66**, 474–478 (2008).
- ²⁶L. Birnbacher, M. Willner, A. Velroyen, M. Marschner, A. Hipp, J. Meiser, F. Koch, T. Schröter, D. Kunka, J. Mohr, F. Pfeiffer, and J. Herzen, “Experimental realisation of high-sensitivity laboratory X-ray grating-based phase-contrast computed tomography,” *Sci. Rep.* **6**, 24022 (2016).
- ²⁷M. Viermetz, L. Birnbacher, M. Willner, K. Achterhold, F. Pfeiffer, and J. Herzen, “High resolution laboratory grating-based X-ray phase-contrast CT,” *Sci. Rep.* **8**, 15884 (2018).
- ²⁸IEC 62220-1:2003(E), “Medical electrical equipment – characteristics of digital X-ray imaging devices – Part 1: Determination of the detective quantum efficiency,” Standard, International Electrotechnical Commission, Geneva, CH, 2003.
- ²⁹A. M. Gurvich, “Luminescent screens for mammography,” *Radiat. Meas.* **24**, 325–330 (1995).
- ³⁰J. D. Kuttig, C. Steiding, D. Kolditz, M. Hupfer, M. Karolczak, and W. A. Kalender, “Comparative investigation of the detective quantum efficiency of direct and indirect conversion detector technologies in dedicated breast CT,” *Phys. Med.* **31**, 406–413 (2015).
- ³¹P. Allé, E. Wenger, S. Dahaoui, D. Schaniel, and C. Lecomte, “Comparison of CCD, CMOS and hybrid pixel x-ray detectors: Detection principle and data quality,” *Phys. Scr.* **91**, 063001 (2016).
- ³²IEC 61267:2005(E), “Medical diagnostic X-ray equipment – radiation conditions for use in the determination of characteristics,” Standard, International Electrotechnical Commission, Geneva, CH, 2005.
- ³³I. A. Cunningham, “Applied linear-systems theory,” in *Handbook of Medical Imaging, Handbook of Medical Imaging No. Bd. 1*, edited by J. Beutel, H. Kundel, and R. Van Metter (Society of Photo Optical Instrumentation Engineers, 2000), pp. 82–155.
- ³⁴J. M. Boone, “X-ray production, interaction, and detection in diagnostic imaging,” in *Handbook of Medical Imaging, Handbook of Medical Imaging No. Bd. 1*, edited by J. Beutel, H. Kundel, and R. Van Metter (Society of Photo Optical Instrumentation Engineers, 2000), pp. 1–78.
- ³⁵H. Kato, “Photon mass energy transfer coefficients for elements Z=1 to 92 and 48 additional substances of dosimetric interest,” *Nihon Hoshasen Gijyutsu Gakkai Zasshi* **70**, 684–691 (2014).
- ³⁶M. Willner, J. Herzen, S. Grandl, S. Auweter, D. Mayr, A. Hipp, M. Chabior, A. Sarapata, K. Achterhold, I. Zanette, T. Weitkamp, A. Sztrókay, K. Hellerhoff, M. Reiser, and F. Pfeiffer, “Quantitative breast tissue characterization using grating-based x-ray phase-contrast imaging,” *Phys. Med. Biol.* **59**, 1557–1571 (2014).
- ³⁷A. Sarapata, M. Chabior, C. Cozzini, J. I. Sperl, D. Bequé, O. Langner, J. Coman, I. Zanette, M. Ruiz-Yaniz, and F. Pfeiffer, “Quantitative electron density characterization of soft tissue substitute plastic materials using grating-based x-ray phase-contrast imaging,” *Rev. Sci. Instrum.* **85**, 103708 (2014).
- ³⁸F. Pfeiffer, C. Kottler, O. Bunk, and C. David, “Hard x-ray phase tomography with low-brilliance sources,” *Phys. Rev. Lett.* **98**, 108105 (2007).
- ³⁹J. C. Larsson, U. Lundström, and H. M. Hertz, “Characterization of scintillator-based detectors for few-ten-keV high-spatial-resolution x-ray imaging,” *Med. Phys.* **43**, 2731–2740 (2016).
- ⁴⁰C. Xu, M. Danielsson, and H. Bornefalk, “Evaluation of energy loss and charge sharing in cadmium telluride detectors for photon-counting computed tomography,” *IEEE Trans. Nucl. Sci.* **58**, 614–625 (2011).
- ⁴¹C. Ponchut, “Correction of the charge sharing in photon-counting pixel detector data,” *Nucl. Instrum. Methods Phys. Res., Sect. A* **591**, 311–313 (2008).